SCIENCE CHINA
Earth Sciences

•RESEARCH PAPER•

July 2022 Vol.65 No.7: 1353–1367
https://doi.org/10.1007/s11430-021-9921-7

Increased water vapor supply in winter and spring leading to the arid Central Asian wetting in last 6000 years

Xu ZHANG[1,2*†], Bo LIU[1†], Shengqian CHEN[2,1], Zhenhao FU[1], Tingting XIE[1] & Fahu CHEN[2,1]

[1] *Key Laboratory of Western China's Environmental Systems (Ministry of Education), College of Earth and Environmental Sciences, Lanzhou University, Lanzhou 730000, China;*
[2] *Alpine Paleoecology and Human Adaption Group (ALPHA), State Key Laboratory of Tibetan Plateau Earth System, Resources and Environment (TPESRE), Institute of Tibetan Plateau Research, Chinese Academy of Science, Beijing 100101, China*

Received July 4, 2021; revised March 8, 2022; accepted March 18, 2022; published online June 6, 2022

Abstract Paleoclimate reconstructions show that the arid Central Asia (ACA) is characterized by a wetting trend from the mid-Holocene (MH) to the Preindustrial period (PI), which has been acknowledged to be a result of increased mean precipitation. However, a systemic understanding of its governing dynamics remains elusive. Based on model outputs from 13 climate models from the Paleoclimate Model Intercomparison Project phase 4 (PMIP4) and proxy records from ACA, here we show that increase in mean precipitation in ACA can be attributed to changes in water vapor source and its transport intensity in winter (December, January, and February) and spring (March, April, and May). In particular, the increase in water vapor supply in winter is associated with the southerly wind anomaly over the northwestern Indian Ocean and Central Asia, caused by an overall weakening of the Asian winter monsoon. This is conducive to water vapor transport from the upwind regions (e.g., Mediterranean) to ACA. Meanwhile, water vapor supply from the eastern Iceland is also enhanced due to a negative North Atlantic Oscillation-like (NAO-like) atmospheric circulation pattern caused by sea ice expansion in the North Atlantic. In spring, evaporation over land and inland lakes is enhanced by increased insolation in the Northern Hemisphere, which increases atmospheric humidity that fuels midlatitude westerlies to enhance ACA precipitation. In addition, weakened atmospheric subsidence over ACA in winter and spring also contributes to the increased precipitation. Overall, our results indicate that paleoclimate modeling is of great importance for disentangling governing dynamics accounting for reconstructed climate phenomena that might be a synergic consequence of several processes operating in different seasons.

Keywords Arid Central Asia, Precipitation, Mid-Holocene, Paleoclimate simulation

Citation: Zhang X, Liu B, Chen S, Fu Z, Xie T, Chen F. 2022. Increased water vapor supply in winter and spring leading to the arid Central Asian wetting in last 6000 years. Science China Earth Sciences, 65(7): 1353–1367, https://doi.org/10.1007/s11430-021-9921-7

1. Introduction

Arid Central Asia (ACA), as controlled by midlatitude westerlies, is the largest nonzonal arid region in the world. Its climatic characteristics are different from those in "Monsoonal Asia" (i.e., East and South Asia), which is dominated by monsoon system (Chen et al., 2019). This region is located in the hinterland of Eurasia, and is characterized by scarce water resources, sparse vegetation cover and fragile ecosystems, which gives rise to its high sensitivity to climate change (Gasse et al., 1991; D'Arrigo et al., 2000; Sorg et al., 2012; Zhang and Feng, 2018). Therefore, great attention has been paid to its spatiotemporal climate and environment changes in different time scales.

The mid-Holocene (MH) is a historical period 6000 years

* Corresponding author (email: xu.zhang@itpcas.ac.cn)
† These authors contributed equally to this work

ago. Its most evident difference from the modern climate is the configuration of the Earth's orbit. Compared with Pre-industrial period (PI), the boreal summer (winter) insolation in the MH was higher (lower), indicating a stronger seasonality (Berger, 1978). There are abundant proxy records used to reconstruct climate change in ACA since the MH. For example, a study based on 12 high-quality lake records revealed that the moisture has decreased in ACA since the MH (Chen et al., 2008, 2009). It is worth noting that some proxy records influenced by the East Asian summer monsoon (EASM) during the early Holocene (EH) to MH were included in that early work, causing erroneous estimates of the moisture evolution in ACA. Recently, Chen et al. (2019) refined the "Westerlies-Dominated Climatic Regime" (WDCR) theoretical framework based on the understanding of climate change in modern midlatitude Asia. Therein they divided the old ACA region into a westerlies-dominated region and a transitional belt between the monsoon- and westerlies-dominated regions. They further pointed out that the moisture in the WDCR core area increased rapidly after the MH, reaching its maximum in the late Holocene. That is, ACA got wetter from the MH to PI, supported by numerous proxy records in the WDCR (e.g., Wang and Feng, 2013; Leroy et al., 2014; Chen et al., 2016; Xu et al., 2019; Li J Y et al., 2020; Wang et al., 2020; Zhang et al., 2020).

Climate models can mimic climate responses caused by changes in Earth's orbit, greenhouse gases, ice sheets, and other climate forcing factors (Kutzbach and Otto-Bliesner, 1982; Prell and Kutzbach, 1987; Joussaume and Braconnot, 1997; Montoya et al., 2000; Kutzbach et al., 2008) and have been widely used for paleoclimate dynamics. Previous modeling work on Holocene climate evolution in ACA mainly focused on the mechanism for the EH drought. For example, Jin et al. (2012) applying the coupled climate model CCSM3.0 proposed that the EH (8.5 ka BP) desertification in ACA was mainly caused by orbital configuration. This orbital setup reduced latitudinal temperature gradient in boreal winter, weakening the midlatitude westerlies and suppressing the upwind evaporation by lowering the temperature. These responses reduced the water vapor transport to ACA, leading to the drought in the EH. In addition, Carlson and Clark (2012) show that stronger boreal summer insolation accelerated ice sheet melting in the Northern Hemisphere, such as the Laurentide Ice Sheet (LIS). This boosts meltwater injection into the North Atlantic, weakening the Atlantic meridional, overturning circulation and hence cooling the northern high latitudes. This further weakens North Atlantic evaporation, reducing the water vapor transport to ACA and hence facilitating the EH ACA desertification (Chen et al., 2019). Based on transient climate simulations of the Kiel Climate Model (KCM), Zhang X J et al. (2016, 2017) confirmed that the persistent Holocene wetting trend in winter in northwestern China is a reflection of the increasing boreal winter insolation in the midlatitudes. They proposed that the increasing winter insolation weakens the East Asian winter monsoon, which is conducive to ACA rainfall, by weakening the Siberian High that is harmful for atmospheric ascending motion. However, climate backgrounds during the EH are distinct from those during MH. That is, stronger boreal seasonality (Berger, 1978), lower atmospheric CO_2 and other greenhouse gas levels (Indermuhle et al., 1999; Monnin et al., 2004; Ruddiman, 2007; Loulergue et al., 2008), and remanent LIS (Carlson et al., 2008) during the EH, disable a simple transfer of governing mechanisms of the early-to-late Holocene precipitation change in ACA to explain changes in the mid-to-late Holocene. Based on multi-model results in PMIP3, Xu et al. (2020) pointed out that the precipitation was higher during the PI than that during the MH, consistent with reconstructions. However, they did not further analyze the associated dynamic mechanisms. In this study, by using model outputs from the latest PMIP4, we explore dynamics accounting for increasing ACA precipitation from the MH to PI.

2. Data and methods

2.1 Study area

The Caspian Sea bounds the western part of the study area, and the eastern part extends to the arid region of Northwest China and Mongolia. The study area spans meridionally by 15° from 35°N to 50°N (Figure 1). It covers five countries (i.e., Kazakhstan, Kyrgyzstan, Tajikistan, Turkmenistan, and Uzbekistan) and a small part of northern Iran, Afghanistan, and Pakistan, as well as northwestern China and western Mongolia.

2.2 Model and datasets

The datasets are from the PMIP4 model simulations. We selected 13 models, including both PI and MH experiments, for the analysis: AWI-ESM-1-1-LR (Sidorenko et al., 2015; Rackow et al., 2018), CESM2 (Danabasoglu et al., 2020), EC-Earth3-LR (Zhang et al., 2021), FGOALS-f3-L (He et al., 2019), FGOALS-g3 (Li L J et al., 2020), GISS-E2-1-G (Kelley et al., 2020), INM-CM4-8 (Volodin et al., 2018), IPSL-CM6A-LR (Boucher et al., 2020), MPI-ESM1-2-LR (Mauritsen et al., 2019), MRI-ESM2-0 (Yukimoto et al., 2019), NESM3 (Cao et al., 2018), NorESM1-F (Guo et al., 2019), and NorESM2-LM (Seland et al., 2020), downloaded from https://esgf-node.llnl.gov/projects/cmip6/. For detailed information on these 13 models, please refer to Table 1. Boundary conditions of the PI and MH are listed in Table 2. The last 100-year average was calculated to represent corresponding climatology. The anomaly between MH and PI was used to represent PI anomaly relative to the MH. To

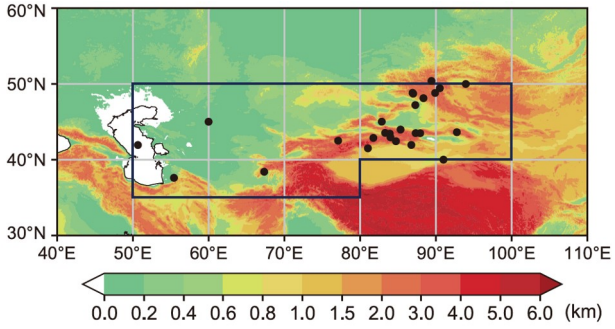

Figure 1 Altitude of Central Asia (in km). The area surrounded by the dark blue solid line is the study area, and the black dots are the spatial locations of the recent proxy records by Chen et al. (2022).

avoid seasonal bias caused by the varying length of the month associated with changing orbital configurations, we corrected model outputs from the default "fixed-day" calendar to a "fixed-angular" calendar (Joussaume and Braconnot, 1997; Chen et al., 2011). In addition, to effectively reduce the model uncertainty, we use the multi-model mean (MMM) to evaluate the climate characteristics and associated dynamic mechanism in ACA. Note that if there are at least seven models consistent with MMM results, MMM is considered to be representative of ACA climate characteristics (e.g., precipitation in Figures 2 and 3), as well as the corresponding physical mechanism. Therefore, if there is no specific description in the following analysis, the variables used meet our criteria for representativeness.

To evaluate model performance on the PI precipitation over ACA, we used the Global Precipitation Climatology Centre (GPCC) dataset from January 1920 to December 2019 with a resolution of 1°×1° (doi: 10.5676/DWD_GPCC/FD_M_V2018_100, download from https://opendata.dwd.de/climate_environment/GPCC/html/fulldata-monthly_v2018_doi_download.html). To evaluate the simulated precipitation anomaly between the MH and PI in PMIP4 models, we employed a new compilation of ACA records, of which details are shown in Table 3 (summarized by Chen et al. (2022)) and Figure 1.

2.3 Vertically integrated water vapor fluxes

To evaluate roles of water vapor supply in ACA precipitation, the vertically integrated water vapor fluxes (unit: kg m^{-1} s^{-1}) can be calculated as follows:

$$Q = \frac{1}{g}\int_{100\text{hPa}}^{P_s} q \cdot V \mathrm{d}p, \tag{1}$$

where g represents gravity acceleration (g=9.8 m s^{-2}), P_s represents surface pressure, q represents specific humidity, V represents horizontal velocity, and Q represents water vapor flux.

To quantify contribution of moisture transport to regional atmospheric water budgets, we calculated the mean annual and seasonal water vapor transport into ACA via each boundary according to the method used by Guan et al. (2019). The calculation formula is as follows:

Western boundary:

$$Q_{\mathrm{W}} = \int_{\varphi_{\mathrm{S}}}^{\varphi_{\mathrm{N}}} Q_{\lambda_{\mathrm{W}}} a \mathrm{d}\varphi. \tag{2}$$

Eastern boundary:

$$Q_{\mathrm{E}} = -\int_{\varphi_{\mathrm{S}}}^{\varphi_{\mathrm{N}}} Q_{\lambda_{\mathrm{E}}} a \mathrm{d}\varphi. \tag{3}$$

Southern boundary:

$$Q_{\mathrm{S}} = \int_{\lambda_{\mathrm{W}}}^{\lambda_{\mathrm{E}}} Q_{\varphi_{\mathrm{S}}} a\cos\varphi_{\mathrm{S}} \mathrm{d}\lambda. \tag{4}$$

Northern boundary:

$$Q_{\mathrm{N}} = -\int_{\lambda_{\mathrm{W}}}^{\lambda_{\mathrm{E}}} Q_{\varphi_{\mathrm{N}}} a\cos\varphi_{\mathrm{N}} \mathrm{d}\lambda, \tag{5}$$

where λ_{W} and λ_{E} represent the longitudes of the western and eastern boundaries, respectively; φ_{S} and φ_{N} represent the latitudes of the southern and northern boundaries, respectively; $Q_{\lambda_{\mathrm{W}}}$ and $Q_{\lambda_{\mathrm{E}}}$ represent the zonal fluxes across the western and eastern boundaries, respectively; and $Q_{\varphi_{\mathrm{S}}}$ and $Q_{\varphi_{\mathrm{N}}}$ represent the meridional fluxes across the southern and northern boundaries, respectively. The value adopted for the Earth's mean radius was a=6.37×10^6 m.

3. Results

3.1 Model evaluation

First, we compared GPCC precipitation with PI results simulated by the 13 selected models. Table 4 shows their correlation coefficients. The results showed that the coefficients were significantly different among models in terms of annual and seasonal precipitation. Among them, MRI-ESM2-0 is characterized by the highest winter (average in December, January, and February) coefficient, while AWI-ESM-1-1-LR features the lowest spring (average in March, April, and May) coefficient (note that correlations exceeding the 95% confidence level but not exceeding the 99% confidence level). Importantly, only six models are characterized by higher-than-MMM correlation coefficients, although mainly for a single season. This indicates that the MMM can better represent and capture observed precipitation patterns than a single model.

3.2 Model-data comparison

In this section, we compare PMIP4 model results with proxy records to evaluate the reliability of the model results (Figure

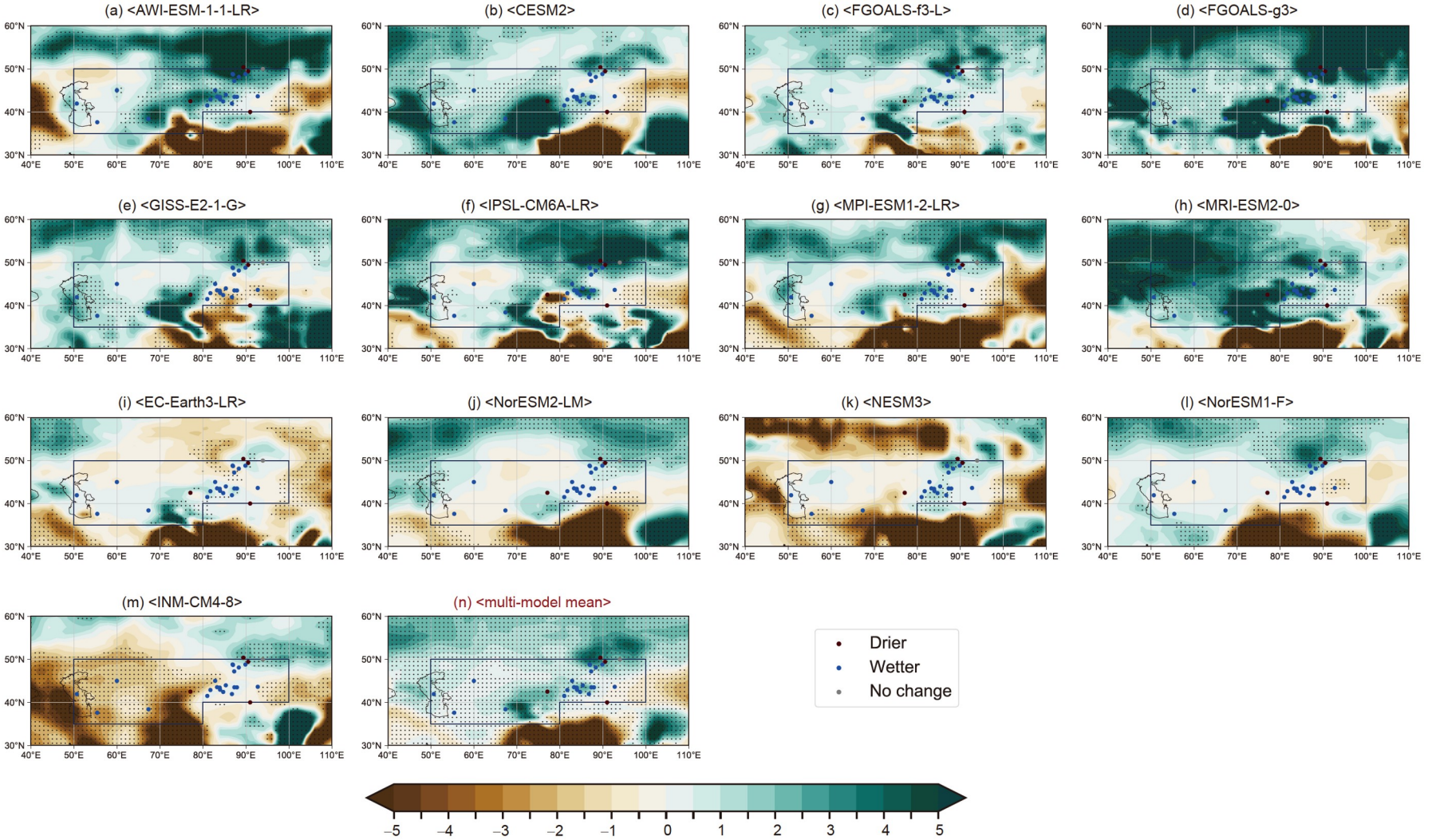

Figure 2 (a)–(m) The anomalies of annual mean precipitation (units: mm/month) between the PI and MH in different models. (n) The MMM of a simulated anomaly in annual mean precipitation (units: mm/month) between PI and MH. The black dots in (a)–(m) represent differences in precipitation between the PI and the MH that are significant at the 95% confidence level. (n) The black dots denote that at least 7 of the 13 models agree with the sign of the MMM. The colored dots in (a)–(n) are the spatial distribution of the proxy records.

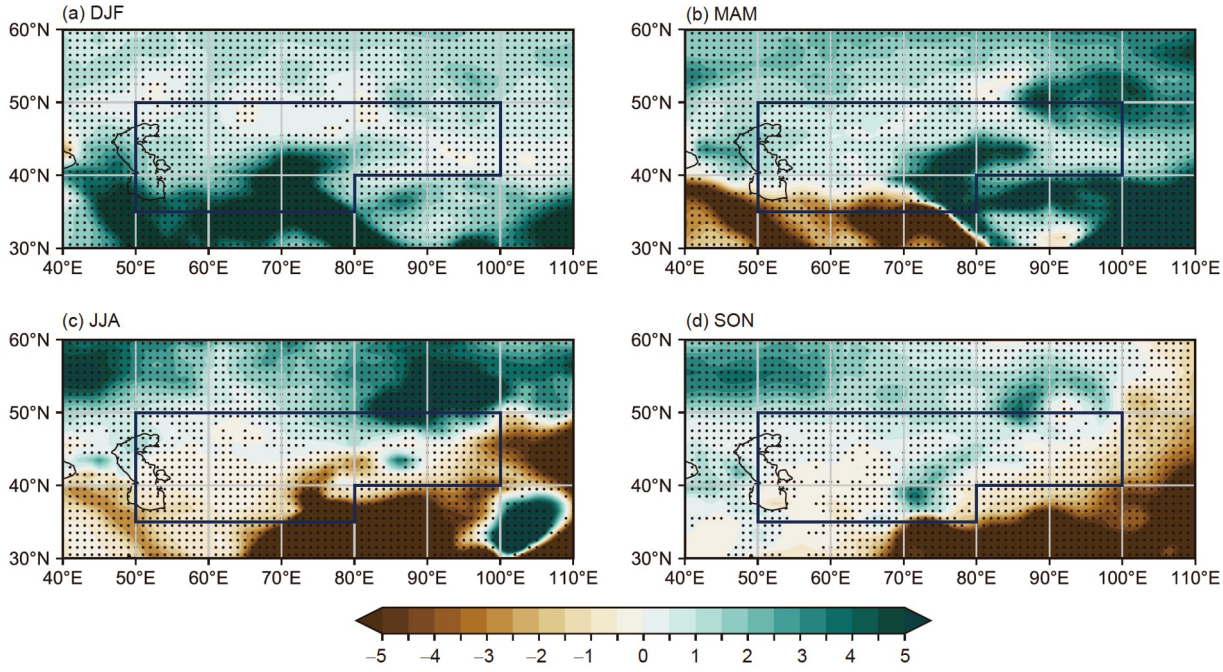

Figure 3 The MMM anomalies of precipitation (units: mm/month) between the PI and the MH in winter (a), spring (b), summer (c), and autumn (d). The black dots indicate that at least 7 of the 13 models agree on the sign of MMM.

Table 1 Model name, spatial resolution and country[a)]

Model name	Atmosphere resolution			Ocean resolution			Country
	Lon	Lat	Level	Lon	Lat	Level	
AWI-ESM-1-1-LR*	192	96	L47	126859 wet nodes#		L46	Germany
CESM2	288	192	L32	320	384	L60	USA
EC-Earth3-LR	320	160	L62	362	292	L75	Sweden
FGOALS-f3-L*	288	180	L32	360	218	L30	China
FGOALS-g3	180	80	L26	360	218	L30	China
GISS-E2-1-G*	144	90	L40	360	180	L40	USA
INM-CM4-8**	180	120	L21	360	318	L40	Russia
IPSL-CM6A-LR	144	143	L79	362	332	L75	France
MPI-ESM1-2-LR	192	96	L47	256	220	L40	Germany
MRI-ESM2-0	320	160	L80	360	364	L61	Japan
NESM3***	192	96	L47	384	362	L46	China
NorESM1-F	144	96	L32	360	384	L70	Norway
NorESM2-LM	144	96	L32	360	384	L70	Norway

a) * denotes a model that lacks the sea ice area percentage and does not include in the calculation of average; ** denotes a model that lacks omega and does not include in the calculation of average; *** denotes a model that lacks evaporation and does not include in the calculation of average; # The grid information of the AWI-ESM-1-1-LR in the ocean model is irregular.

2). Since the proxy records mainly reflect the annual mean (Chen et al., 2022), we use simulated annual mean precipitation in this analysis.

Of thirteen models eight (Figure 2a–2h, corresponding to AWI-ESM-1-1-LR, CESM2, FGOALS-f3-L, FGOALS-g3, GISS-E2-1-G, IPSL-CM6A-LR, MPI-ESM1-2-LR, and MRI-ESM2-0, respectively) are characterized with increasing ACA precipitation from the MH to PI, with majority of the ACA area exceeding 95% confidence level. Four models (Figure 2i–2l, corresponding to EC-Earth3-LR, NorESM2-LM, NESM3, and NorESM1-F respectively) simulated precipitation reduction in a large part of plotted area, but in ACA area their increased precipitation is significant (exceeding the 95% confidence level). Only INM-CM4-8 (Figure 2m) characterizes a general decrease in precipitation. Figure 2n shows the comparison between the MMM and

Table 2 Orbital parameters and greenhouse gases for the PI and MH experiments[a)]

Boundary conditions	PI	MH
Eccentricity	0.016764	0.018682
Obliquity (°)	23.459	24.105
Perihelion-180° (°)	100.33	0.87
Carbon dioxide (ppm)	284.3	264.4
Methane (ppb)	808.2	597
Nitrous oxide (ppb)	273	262
Solar constant (W m^{-2})	1360.747	PI

a) https://pmip4.lsce.ipsl.fr/. 1 ppm=10^{-6}, 1 ppb=10^{-9}.

proxy records. It appears that the MMM precipitation in ACA is characterized by a significant increase during the PI, in good agreement with the reconstructed moisture change.

This analysis suggests that there exists a large spread on simulated ACA precipitation change while the MMM can effectively reduce these model uncertainty and thus improve their consistency with proxy records.

3.3 Precipitation seasonal variability

We further analyzed the precipitation seasonality to clarify dynamic mechanisms accounting for mean annual precipitation change. The MMM indicates that seasons with the most significant precipitation increase in ACA are winter (Figure 3a) and spring (Figure 3b). Therein regions between Pamir Plateau and the Caspian Sea are characterized by significant rainfall increase in winter (Figure 3a), while in spring, the significant regions are just over Pamir Plateau and Tianshan Mountains (Figure 3b). Rainfall in summer was significantly reduced, in contrast to winter, spring, and annual mean (Figure 3c). Simulated rainfall change in autumn is in general in line with annual mean but with a weak magnitude and thus a weak contribution to annual mean (Figure 3d).

Table 3 Proxy records in ACA, summarized from Chen et al. (2022)[a)]

Site name	Latitude	Longitude	Moisture conditions	Proxies used	References
Lake Issyk-Kul	42.50°N	77.10°E	Drier	$\delta^{18}O$, $CaCO_3$, pollen	Rasmussen et al., 2001; Ricketts et al., 2001; Ferronskii et al., 2003
Lake Bosten	41.94°N	86.76°E	Wetter	Pollen	Wünnemann et al., 2006; Huang et al., 2009
Lake Akkol	50.38°N	89.42°E	Drier	Pollen	Blyakharchuk et al., 2007
Lake Wulungu	47.20°N	87.29°E	Wetter	Grain size, pollen	Liu et al., 2008
Aral Sea	45.00°N	60.00°E	Wetter	Terrace, historical documents	Krivonogov et al., 2010
Lake Balikun	43.62°N	92.77°E	Wetter	Pollen	Tao et al., 2010; An et al., 2012
Lake Sayram	41.50°N	81.03°E	Wetter	Pollen	Jiang et al., 2013
Lake Achit Nur	49.42°N	90.52°E	Drier	Pollen	Sun et al., 2013
Lake Aibi	45.01°N	82.86°E	Wetter	Pollen	Wang et al., 2013
Chaiwobu Peatland	43.49°N	87.93°E	Wetter	Cellulose $\delta^{13}C$ value	Hong et al., 2014
Caspian Sea	41.93°N	50.67°E	Wetter	Pollen	Leroy et al., 2014
Lake Bayan Nur	49.98°N	93.95°E	No change	Pollen	Tian et al., 2014
Kansu section	43.43°N	83.92°E	Wetter	Magnetic proxies	Chen et al., 2016
Lujiaowan section	43.97°N	85.34°E	Wetter	Magnetic proxies	Chen et al., 2016
Zeketai section	43.53°N	83.30°E	Wetter	Magnetic proxies	Chen et al., 2016
Zhongliang section	43.50°N	87.33°E	Wetter	Magnetic proxies	Chen et al., 2016
Kesang Cave	42.87°N	81.75°E	Wetter	trace element ratios, $\delta^{18}O$	Cheng et al., 2016; Cai et al., 2017
Ton Cave	38.4°N	67.34°E	Wetter	trace element ratios, $\delta^{18}O$	Cheng et al., 2016
Lake Lup Nur	40.00°N	91.00°E	Drier	Grain-size, pollen, ostracod, soluble salt	Liu et al., 2016
TLSH Peatland	48.81°N	86.92°E	Wetter	Pollen, *n*-alkane	Zhang Y et al., 2016, 2018
NRX Peatland	48.80°N	89.90°E	Wetter	Pollen	Feng et al., 2017
Bayanbulak Basin	42.95°N	84.00°E	Wetter	Grain-size, magnetic susceptibility, loss on ignition	Long et al., 2017
Lake Kanas	48.70°N	87.01°E	Wetter	Pollen	Huang et al., 2018
Baluke Cave	42.43°N	84.73°E	Wetter	trace element ratios, $\delta^{18}O$	Liu et al., 2019, 2020
YE section	37.60°N	55.43°E	Wetter	$\delta^{13}C$	Wang et al., 2020
Kelashazi Peat	48.11°N	88.36°E	Wetter	Pollen	Wang and Zhang, 2019

a) Moisture conditions represent the PI change relative to the MH.

Table 4 Correlation coefficients between ACA precipitation climatology during the PI simulated by the 13 models and the observed precipitation climatology (1920–2019) from the GPCC[a)]

Models	ANN	DJF	MAM	JJA	SON
AWI-ESM-1-1-LR	0.349	0.663	0.085*	0.431	0.567
CESM2	0.520	0.672	0.527	*0.745*	0.449
EC-Earth3-LR	0.573	0.388	*0.788*	0.590	0.477
FGOALS-f3-L	0.542	0.654	0.501	0.468	0.387
FGOALS-g3	0.537	0.513	0.490	0.577	0.464
GISS-E2-1-G	0.318	0.367	0.444	0.469	0.266
INM-CM4-8	0.388	0.516	0.118	*0.714*	0.335
IPSL-CM6A-LR	*0.686*	0.707	*0.661*	0.690	0.590
MPI-ESM1-2-LR	0.592	0.550	*0.593*	0.581	0.559
MRI-ESM2-0	*0.730*	*0.842*	*0.776*	0.704	0.568
NESM3	0.451	0.708	0.286	0.461	0.565
NorESM1-F	0.175	0.341	0.151	0.497	0.258
NorESM2-LM	0.559	0.708	0.291	0.640	0.595
MMM	*0.605*	*0.727*	*0.579*	*0.708*	*0.628*

a) The result of the MMM is the correlation between the mean values of the 13 models and the GPCC. * denotes correlations exceeding the 95% confidence level; the others exceed the 99% confidence level. The correlation coefficients greater than the MMM are italicized, with ANN representing the annual mean, DJF representing the average of December, January, and February, MAM representing the average of March, April, and May, JJA representing the average of June, July and August, and SON representing the average of September, October, and November.

3.4 Water vapor supply in winter and spring

As indicated by the seasonal variability of precipitation (Figure 3), the mean annual precipitation increase is mainly associated with winter and spring precipitation increase. Of particular relevance to ACA precipitation is atmospheric water vapor content (Zhang X J et al., 2016). Climatologically, the ACA water vapor mainly comes from upwind evaporation over the North Atlantic, inland seas, and lakes, which is transported to ACA by the midlatitude westerlies (Figure 4a, 4c; Böhner, 2006; Zhang, 2021). Therefore, the physical mechanism causing precipitation increase in winter and spring during the PI can be attributed to changes in pathway and intensity of water vapor transport. In this section, we explore the reasons for these changes in winter and spring between the PI and MH.

In winter, there exist two anomalous water vapor transports, accounting for increased precipitation in ACA (Figure 4b). One transport anomaly is northward water vapor transport from the northwestern tropical Indian Ocean to the ACA. Based on the climatological water vapor transport during the MH (Figure 4a), this indicates that water vapor from upwind areas of ACA (such as the Mediterranean) tends not to be transported to the Indian Ocean, but rather to ACA. The other represents a water vapor source originating from the ocean in east of Iceland, which goes southeastwards across the Western Europe and the Mediterranean, turning eastwards over the northeastern North Africa and then merging with the southerly water vapor in south of Iranian Plateau. The merged water vapor finally enters ACA from the western of the southern boundary of the study area (i.e., the Iranian Plateau and other places) (Table 5). This accounts for a significant increase in precipitation mainly in the south of the study area (Figure 3a).

Moisture supply for ACA precipitation in spring is different from that in winter (Figure 4d). In comparison to the MH, more water vapor is transported eastwards from the North Atlantic to the Eurasian continent at mid-latitudes during the PI (Figure 4d). After passing the mid Europe, the water vapor turns southwards towards the eastern Mediterranean Sea, where part of it turns eastwards via Caspian Sea to ACA (Figure 4d; Table 5). This finally provides extra water vapor for increased ACA precipitation in ACA in spring (Figure 3b).

4. Underlying dynamics

The increased water vapor import strengthens ACA precipitation in winter and spring in the last 6000 years. Changes in water vapor transport are a consequence of atmospheric humidity and large-scale atmospheric circulation. In this section, we investigate these two controlling factors to account for an underlying dynamic of the increasing ACA precipitation in winter and spring from the MH to PI.

4.1 Dynamic mechanism of winter precipitation variations

Climatologically, boreal midlatitude westerlies transport

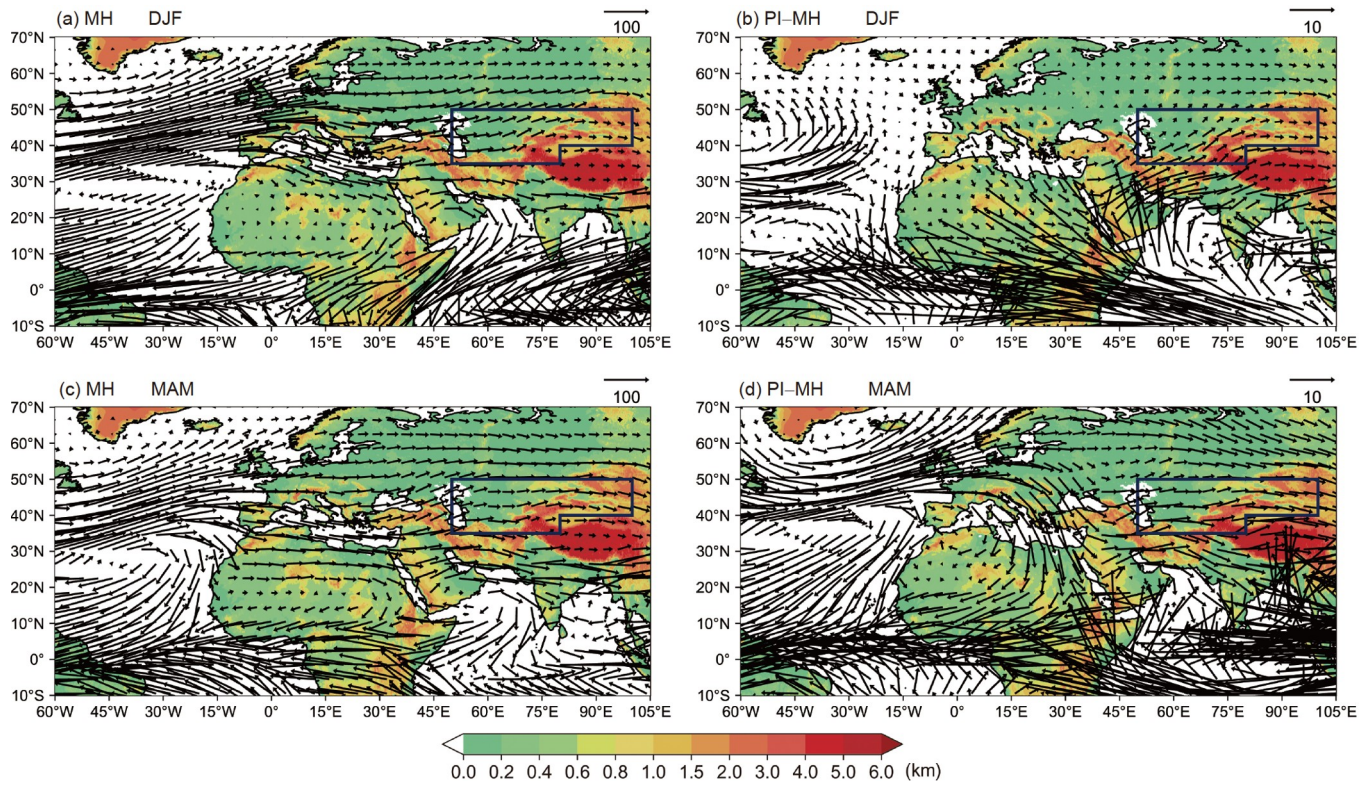

Figure 4 The MMM vertical integrated water vapor transport (arrow; unit: kg m^{-1} s^{-1}) for the MH in winter (a) and its anomaly (arrow; unit: kg m^{-1} s^{-1}) between the PI and the MH (b); (c) same as (a) but in spring; (d) same as (b) but in spring. Color shadings indicate the elevation (in km) of the terrain.

Table 5 MMM anomaly of vertical integrated water vapor transport between the PI and the MH at each boundary of the study area in winter and spring

Season	Western boundary (50°E, 35°N–50°N)	Eastern boundary		Southern boundary		Northern boundary (50°E–100°E, 50°N)	Regional atmospheric water budgets
		Northern part (100°E, 40°N–50°N)	Southern part (80°E, 35°N–40°N)	Western part (50°E–80°E, 35°N)	Eastern part (80°E–100°E, 40°N)		
Winter ($\times10^{10}$ kg s^{-1})	1.60	−1.58	−1.19	3.25	0.04	−1.13	0.99
Spring ($\times10^{10}$ kg s^{-1})	6.39	−3.79	−2.38	0.20	−0.51	0.15	0.05

water vapor to ACA from the North Atlantic, Mediterranean, and the Caspian Sea in winter (Figure 4a; Böhner, 2006; Guan et al., 2019; Zhang, 2021). This process provides sufficient water vapor for winter precipitation, resulting in a high proportion of winter precipitation in the annual precipitation (Guan et al., 2019; Zhang, 2021). However, the Eurasian continent is mainly controlled by the downdraft generated by Siberian High, suppressing ACA precipitation (Zhang X J et al., 2016). The modeling results show that changes in the Earth's precession (Table 2) increase boreal winter insolation from the MH to PI (Berger, 1978). Due to the lower specific heat capacity over land than in the sea, the boreal temperature over land in winter was approximately 1°C higher than that over the Indian Ocean and the Pacific Ocean during the PI (Figure 5a). This reduces the land-sea temperature difference, weakening the Asian winter monsoon and hence resulting in a southerly wind anomaly over the northwestern Indian Ocean and south of Central Asia (Figure 5d). This effectively reduces water vapor import into the tropical Indian Ocean, promoting the upwind water vapor transport to ACA and hence strengthening the ACA precipitation. Xie et al. (2021) by investigating mechanisms of interannual winter rainfall in southern ACA during 1979 to 2017, found that southerly anomaly can bring more water vapor from the Arabian Sea, leading to the occurrence of modern extreme precipitation events inland. In addition, the land-sea temperature response also modulates large scale atmospheric circulation (Figure 5a, 5b): weakened Siberian High over Central Asia, and positive sea level pressure anomalies over the tropical southern Indian Ocean (Figure 5b). It appears that the center of the positive 200 hPa geopotential height (GPH) anomaly lies in the Asian continent, while the tropical Indian Ocean experiences a slight increase in the GPH field (Figure 5a). This spatial configuration of the

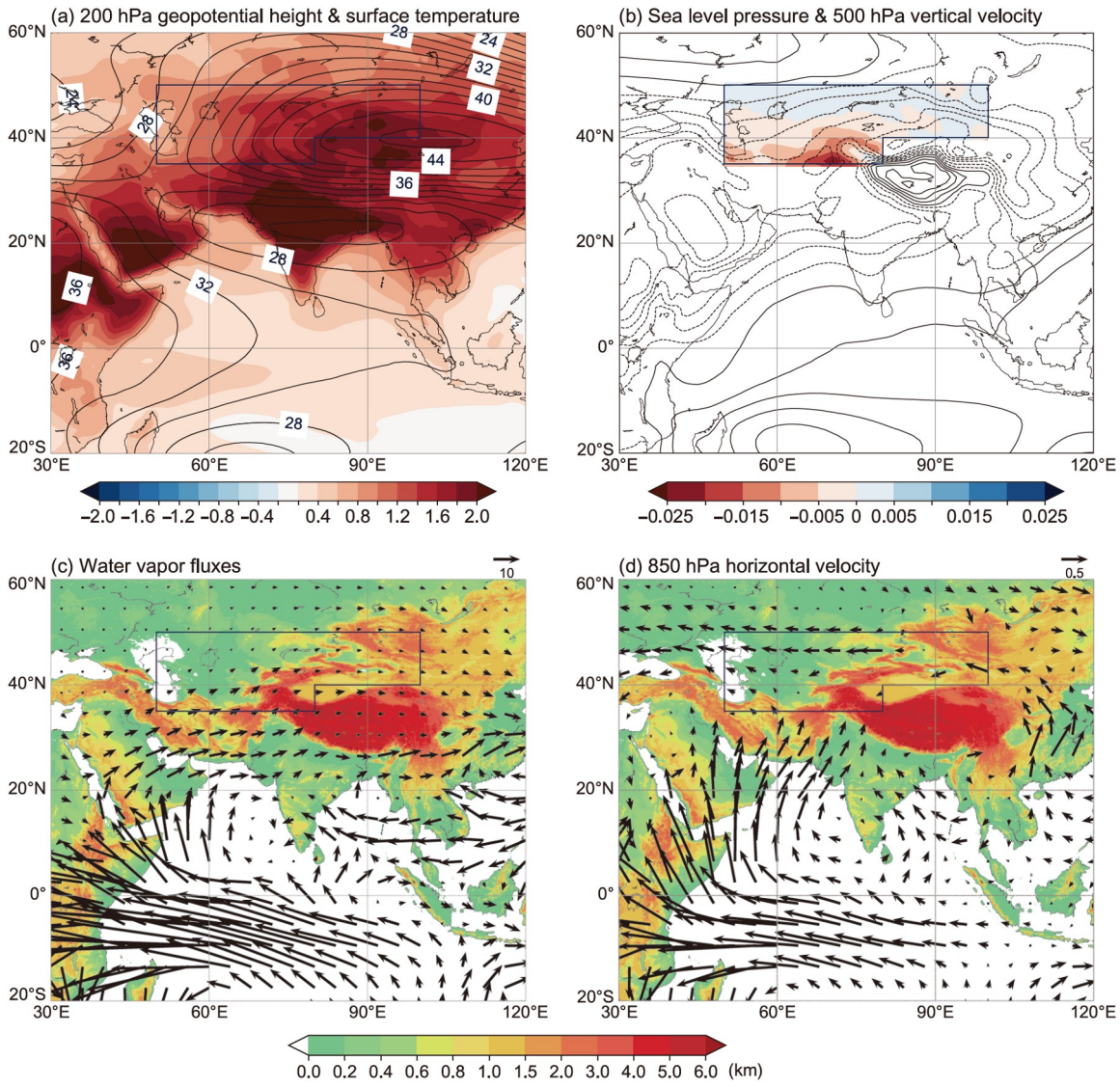

Figure 5 The MMM anomalies of (a) 200 hPa geopotential height (contour; unit: m) and surface temperature (color shading; unit: °C), (b) sea-level pressure (contour; unit: Pa) and 500 hPa vertical velocity (color shading; unit: Pa s^{-1}), (c) water vapor fluxes (arrows; unit: kg m^{-1} s^{-1}), and (d) 850 hPa horizontal velocity (arrows; unit: m s^{-1}) between the PI and MH in winter. Contour intervals are 2 m and 20 Pa in (a) and (b), respectively. The solid lines in (a), (b) indicate positive values, and the dotted lines indicate negative values, and a negative value for vertical velocity in (b) indicates uplift. The color shading indicates the elevation (in km) of the terrain in (c), (d).

pressure field weakens the strength of the Siberian High, reducing the atmospheric subsidence movement over the ACA, especially its southern region (Figure 5b), and hence generating conditions favorable for ACA precipitation. This is also supported by modeling results in Zhang X J et al. (2016) which suggested a weakening of the East Asian winter monsoon intensity since the MH. In addition, they calculated correlation between the East Asian winter monsoon intensity and the winter precipitation in Northwest China, which exhibits a significant negative value (r=−0.81, p<0.05) from the MH to PI.

Since the ACA is sensitive to change in atmospheric moisture, an increase in water vapor transport from the sea in east of Iceland also plays a role in ACA precipitation, although its amount is relatively smaller in comparison with that from the tropical Indian Ocean. The increasing precession from the MH to PI reduces boreal summer insolation (Berger, 1978), which can give rise to an increase in mean annual sea ice at northern high latitudes (Wu et al., 2020). In winter, regions within Arctic Circle experience polar night and hence local insolation plays a minor role in contemporary sea ice change. Instead, it mainly follows summer sea ice change caused by summer insolation change, as indicated by more extended sea ice cover in eastern Greenland during the PI than that during the MH (Figure 6a). In contrast, sea ice in the south of Arctic Circle is controlled by increasing winter solar insolation, and hence characterized by a significant weakening trend since the MH (Figure 6a).

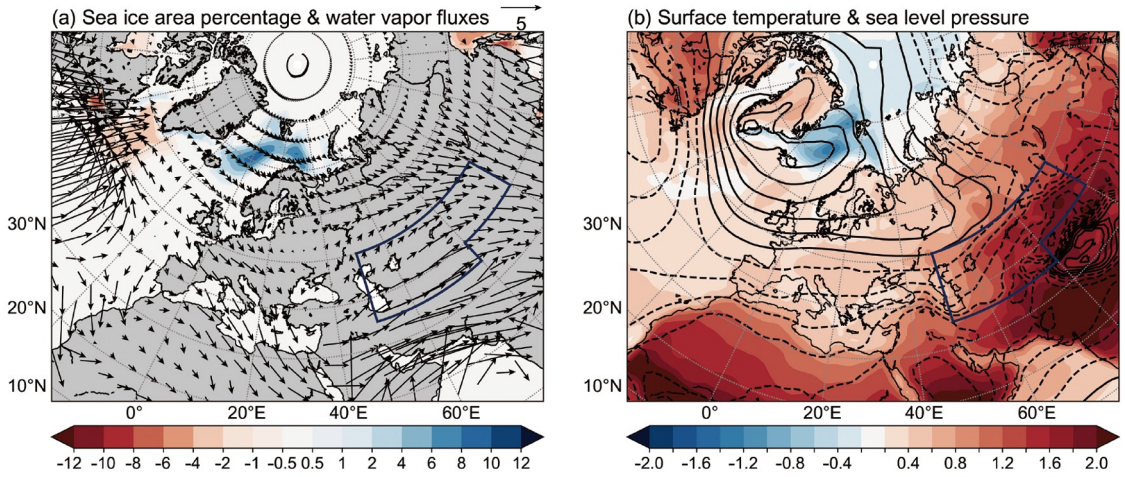

Figure 6 The MMM anomalies of (a) sea ice area percentage (color shading; unit: %) and water vapor fluxes (arrows; unit: kg m^{-1} s^{-1}), (b) surface temperature (color shading; unit: °C) and sea-level pressure (contour; unit: Pa) between the PI and MH in winter. The contour interval is 20 Pa in (b). The solid lines in (b) indicate positive values, and the dotted lines indicate negative values.

This further affects spatial patterns of sea surface temperature and sea-level pressure (Figure 6b). It appears that the Icelandic Low weakened and the Azores High strengthened from the MH to PI, resembling the negative phase of the North Atlantic Oscillation (NAO) (Figure 6b). That is, a NAO-negative phase like climatology pattern. This promotes more water vapor from the northern North Atlantic transported southeastwards via mid-south Europe, which turns eastwards over Northeast Africa to fuel the ACA precipitation (Figure 6a). Our results are supported by previous modeling studies (Lorenz et al., 2006; Zhang et al., 2010; Yuan et al., 2014) and paleoclimate reconstruction regarding the Holocene NAO (Davis et al., 2003; Rimbu et al., 2003, 2004; Olsen et al., 2012). Previous studies have shown that there is an inverse phase relationship between NAO/AO and the ACA winter precipitation on the interannual to centennial timescale (Aizen et al., 2001; Chen et al., 2010). In other words, the positive and negative sea-level pressure anomalies, respectively, in the high and middle latitudes of NAO show a negative NAO/AO atmospheric circulation pattern, which is favorable for ACA precipitation (Li and Wang, 2003; Huang et al., 2013; Kutzbach et al., 2014). Our results are consistent with this view; that is, the North Atlantic atmospheric circulation pattern is characterized by a trend to a negative phase from the MH to the PI. This is conducive to the transport of water vapor from the eastern Iceland to ACA over the European continent, thereby promoting the increase in winter precipitation.

4.2 Dynamic mechanism of spring precipitation variations

Different from the winter case, water vapor import in ACA in spring is mainly attributed to the enhancement of water vapor transport from the upwind area. This is associated with an insolation-induced increase in evaporation in the Mediterranean, continental Europe, and inland water bodies (such as the Black Sea, Caspian Sea, etc.) (Figure 7a), which increases atmospheric humidity (Figure 7b) and hence promotes water vapor transport to ACA (Figure 7b). Enhanced eastward water vapor transport over the North Atlantic is mainly a result of the intensification of the midlatitude westerlies (Figure 7a), serving as the upwind water vapor source for downstream regions (e.g., the European continent) (Figure 7b).

To quantify the source of imported water vapor, we define two upwind regions; subregion R1 (0°E–50°E, 35°N–50°N, representing the Mediterranean and southern Europe) and subregion R2 (60°W–0°, 40°N–60°N, representing the North Atlantic) (Figure 7). Then calculated are the vertically integrated water vapor fluxes across the boundaries of each subregion (Table 6).

The results show that water vapor transport into and out of each subregion is mainly through their western and eastern boundary, respectively (Figure 7; Table 6). Importantly, the water vapor import of subregion R2/R1 is stronger/weaker than its export, indicating that subregion R2/R1 is a sink/source of water vapor. Therefore, the enhanced water vapor transport to ACA during the PI is closely associated with the increased atmospheric humidity caused by the enhanced evaporation over Europe, western Asia and their inland lakes. Meanwhile, increased atmospheric humidity in subregion R2 is a result of the enhanced import of water vapor from North America by midlatitude westerlies, which also accounts for increased water vapor transport from subregion R2 to subregion R1 (Figure 7; Table 6). Overall, the insolation-induced increase in spring water vapor import to ACA can be attributed to the enhanced evaporation over land

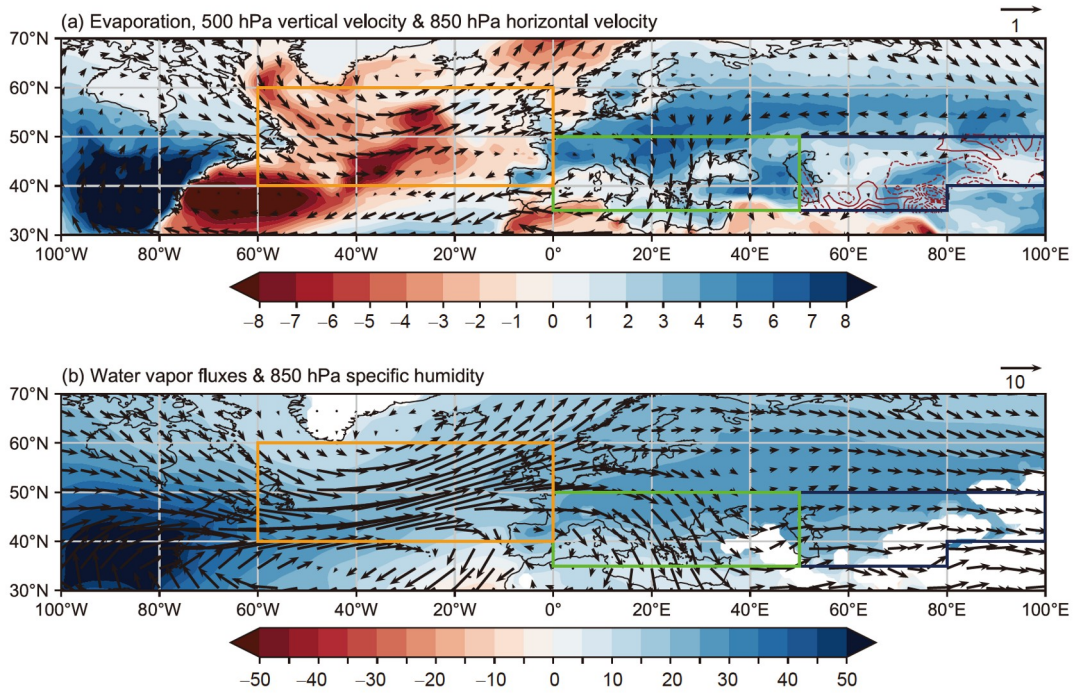

Figure 7 The MMM anomalies of (a) evaporation (color shading; unit: mm/month), 500 hPa vertical velocity (contour; unit: Pa s^{-1}) and 850 hPa horizontal velocity (arrow; unit: m s^{-1}), (b) water vapor flux (arrows; unit: kg m^{-1} s^{-1}) and 850 hPa specific humidity (color shading; unit: 10^{-2} g kg^{-1}) between the PI and MH in spring. ACA is highlighted by the dark blue solid line. Two upwind subregions are defined, solid green and yellow rectangles represent the subregions R1 and R2, respectively. In ACA of subplot (a), contours represent 500 hPa vertical velocity. The contour interval is 0.003 Pa s^{-1}, solid and dotted lines indicate positive (subsident movement) and negative (uplift movement) values.

Table 6 MMM anomaly (PI–MH) of vertically intergrated water vapor flux at each boundary of the two subregions in spring

Subregion	Western boundary	Eastern boundary	Southern boundary	Northern boundary	Regional atmospheric water budgets
R1	3.68	−6.39	−8.36	3.52	−7.55
R2	13.97	−9.60	−0.20	−2.49	1.67

a) The spatial extent of each subregion is shown in Figure 7, unit: $\times 10^{10}$ kg s^{-1}.

and inland lakes in the Northern Hemisphere, support by Jin et al. (2012), which proposed high spring insolation strengthens evaporation in the upstream continental regions in the cold-season of the Northern Hemisphere.

In addition, it appears that the midlatitude westerlies have a weak effect on the enhancement of ACA water vapor import (Figure 7a). In subregion R1 northerly anomaly prevails, although the westerly anomaly prevails in subregion R2 (Figure 7a). Based on eq. (1), the integrated water vapor transport is a function of wind and atmospheric humidity. Therefore, the latter dominates the ACA water vapor import in spring. In other words, enhanced ACA water vapor import is a consequence of increased atmospheric water vapor content caused by strengthened evaporation in its upstream regions.

Finally, the reduced atmospheric subsident movement during the PI, as indicated by the negative anomaly of 500 hPa vertical velocity over ACA (Figure 7a), is a local factor conducive to the increased spring precipitation.

5. Discussions

The ACA drought conditions in the EH have been attributed to a weakened midlatitudes westerlies and reduced evaporation in winter, resulting in a reduction in water vapor supply from the North Atlantic, Caspian Sea, and Mediterranean Sea (Chen et al., 2008, 2016; Liu et al., 2009, 2014; Jin et al., 2012; Wang and Feng, 2013; Zhang X J et al., 2016, 2017). The former might be associated with a decreased meridional temperature gradient caused by insolation change. In addition to low winter insolation, the latter might be attributed to the remnant LIS and the associated meltwater into the North Atlantic (Carlson and Clark, 2012; Jin et al., 2012). Accordingly, Chen et al. (2019) proposed a dynamic framework of "Westerlies-Dominated Climatic Regime", within which changes in midlatitude westerlies across the Holocene can be used to explain the difference in the Holocene precipitation evolution between ACA and East Asian monsoon regions. In addition, insolation-induced enhance-

ment of Siberian High (Zhang X J et al., 2016, 2017) and the negative phase of Arctic Oscillation (AO) or NAO-like atmospheric circulation (Chen et al., 2016) are proposed to explain the ACA drought in the EH.

In this study, we further investigated the underlying dynamics of ACA wetting from the MH to PI based on results from 13 PMIP4 models. Our results show that the wetting is caused by enhanced water vapor supply in both winter and spring. A conceptual diagram has been provided to illustrate the dynamics (Figure 8). In winter, the increased water vapor supply is associated with anomalous southerly over the northwestern Indian Ocean and southern Central Asia and a negative NAO/AO-like atmosphere circulation. The former promotes the water vapor transport from the Mediterranean to ACA, meanwhile, the latter enhanced water vapor transport from the northern North Atlantic to ACA (Figure 8a). In spring, the increased water vapor transported to ACA was mainly related to increased atmospheric humidity as a consequence of enhanced solar insolation (Figure 8b).

Different from the previous view, change in the midlatitude westerlies contributed little to the enhanced water vapor supply in both winter and spring (Figures 6 and 7). The midlatitude westerlies might be weakened by the negative NAO-like phase in winter (Figure 6a; Kutzbach et al., 2014; Orme et al., 2021). The regionally strengthened westerlies only account for the increased water vapor transport from the North Atlantic to the European continent and other places (Figure 7). In contrast, the enhanced transport of water vapor from the European continent to ACA is mainly associated with the insolation-induced increase in evaporation and hence atmospheric humidity (Figure 7a). Therefore, we suggest that the increasing ACA precipitation in the last 6000 years might be mainly caused by changes in water vapor supply due to contemporary insolation increase.

Our findings improve previous dynamic understanding of precipitation change in the "Westerlies-Dominated Climatic Regime" across the Holocene. On one hand, the longitudinal heterogeneity of changes in the midlatitude westerly shown by PMIP4 MMM casts doubt on reliability of using globally zonal mean change to represent regional changes (e.g., in ACA). On the other hand, the proposed mechanisms in this study are different from those inferred from analysis between EH and PI, suggesting that governing dynamics of ACA precipitation change through the Holocene might change with time. This might be a result of change in climate backgrounds. In comparison with the EH, the MH is characterized by an increased winter insolation (Berger, 1978), LIS meltaway (Carlson et al., 2008), and decreased atmospheric CO_2 levels (Indermuhle et al., 1999; Monnin et al., 2004; Ruddiman, 2007; Loulergue et al., 2008).

6. Conclusion

Using modeling results from 13 models in the PMIP4, we explored the governing mechanism of the ACA wetting from the MH to PI. The key findings and conclusions can be summarized as follows.

(1) Increase in ACA precipitation from the MH to PI is closely related to a strengthened water vapor supply in winter and spring; meanwhile, weakening of atmospheric subsidence also plays a positive role.

(2) In winter, two water vapor transport anomalies account for the enhanced moisture supply to ACA since the MH. One is related to the southerly wind anomaly over the northwestern Indian Ocean and Central Asia, as a consequence of weakened Asian winter monsoon caused by enhanced boreal winter insolation. The other is from the region to the east of Iceland to ACA, associated with the negative-phase NAO-like atmospheric circulation pattern, as a consequence of increased winter sea ice caused by the weakened boreal summer insolation.

(3) In spring, the enhanced water vapor supply to ACA is controlled by increased northern hemisphere atmospheric humidity. Increasing boreal spring insolation from the MH to PI promotes continental (and terrestrial lakes and seas)

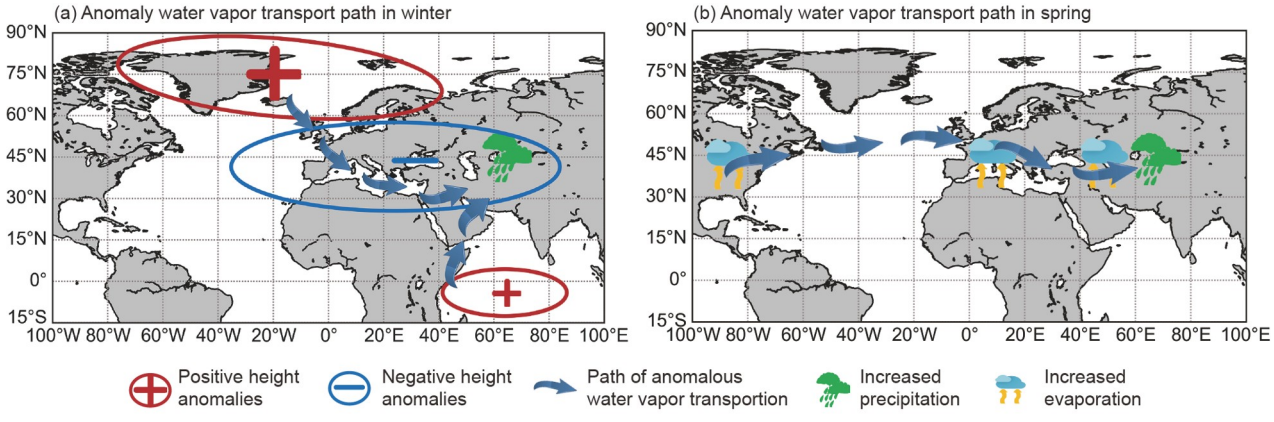

Figure 8 Schematic diagram for governing dynamics of increased water vapor supply to ACA in (a) winter and (b) spring from the MH to PI.

evaporation, increasing air humidity and hence providing more water vapor for ACA precipitation during the PI.

In summary, climatic information derived from reconstructed records might be a consequence of a synergy of multiple dynamical processes and hence possesses different dynamic solutions. Therefore, in a future study, with the aid of high resolution proxy records, climate models and perhaps regional climate models shall be used to deepen our understanding of a tempo-spatial moisture evolution in ACA through the Holocene.

Acknowledgements *The authors thank the International Climate Modeling Group for the analytical data and two anonymous reviewers for their comments and suggestions. This work was supported by the National Program on Key Basic Research Project of China (Grant No. 2018YFA0606403)*

References

Aizen E M, Aizen V B, Melack J M, Nakamura T, Ohta T. 2001. Precipitation and atmospheric circulation patterns at mid-latitudes of Asia. Int J Climatol, 21: 535–556

An C B, Lu Y B, Zhao J J, Tao S C, Dong W M, Li H, Jin M, Wang Z L. 2012. A high-resolution record of Holocene environmental and climatic changes from Lake Balikun (Xinjiang, China): Implications for Central Asia. Holocene, 22: 43–52

Berger A L. 1978. Long-term variations of daily insolation and quaternary climatic changes. J Atmos Sci, 35: 2362–2367

Blyakharchuk T A, Wright H E, Borodavko P S, van der Knaap W O, Ammann B. 2007. Late Glacial and Holocene vegetational history of the Altai Mountains (southwestern Tuva Republic, Siberia). Palaeogeogr Palaeoclimatol Palaeoecol, 245: 518–534

Böhner J. 2006. General climatic controls and topoclimatic variations in Central and High Asia. Boreas, 35: 279–295

Boucher O, Servonnat J, Albright A L, Aumont O, Balkanski Y, Bastrikov V, Bekki S, Bonnet R, Bony S, Bopp L, Braconnot P, Brockmann P, Cadule P, Caubel A, Cheruy F, Codron F, Cozic A, Cugnet D, D'Andrea F, Davini P, Lavergne C, Denvil S, Deshayes J, Devilliers M, Ducharne A, Dufresne J L, Dupont E, Éthé C, Fairhead L, Falletti L, Flavoni S, Foujols M A, Gardoll S, Gastineau G, Ghattas J, Grandpeix J Y, Guenet B, Guez L E, Guilyardi E, Guimberteau M, Hauglustaine D, Hourdin F, Idelkadi A, Joussaume S, Kageyama M, Khodri M, Krinner G, Lebas N, Levavasseur G, Lévy C, Li L, Lott F, Lurton T, Luyssaert S, Madec G, Madeleine J B, Maignan F, Marchand M, Marti O, Mellul L, Meurdesoif Y, Mignot J, Musat I, Ottlé C, Peylin P, Planton Y, Polcher J, Rio C, Rochetin N, Rousset C, Sepulchre P, Sima A, Swingedouw D, Thiéblemont R, Traore A K, Vancoppenolle M, Vial J, Vialard J, Viovy N, Vuichard N. 2020. Presentation and evaluation of the IPSL-CM6A-LR. J Adv Model Earth Syst, 12: e2019MS002010

Cai Y J, Chiang J C H, Breitenbach S F M, Tan L C, Cheng H, Edwards R L, An Z S. 2017. Holocene moisture changes in western China, Central Asia, inferred from stalagmites. Quat Sci Rev, 158: 15–28

Cao J, Wang B, Yang Y M, Ma L B, Li J, Sun B, Bao Y, He J, Zhou X, Wu L G. 2018. The NUIST earth system model (NESM) version 3: Description and preliminary evaluation. Geosci Model Dev, 11: 2975–2993

Carlson A E, Clark P U. 2012. Ice sheet sources of sea level rise and freshwater discharge during the last deglaciation. Rev Geophys, 50: RG4007

Carlson A E, Legrande A N, Oppo D W, Came R E, Schmidt G A, Anslow F S, Licciardi J M, Obbink E A. 2008. Rapid early Holocene deglaciation of the Laurentide Ice Sheet. Nat Geosci, 1: 620–624

Chen F H, Chen J H, Holmes J, Boomer I, Austin P, Gates J B, Wang N L, Brooks S J, Zhang J W. 2010. Moisture changes over the last millennium in arid Central Asia: A review, synthesis and comparison with monsoon region. Quat Sci Rev, 29: 1055–1068

Chen F H, Chen J H, Huang W, Chen S Q, Huang X Z, Jin L Y, Jia J, Zhang X J, An C B, Zhang J W, Zhao Y, Yu Z C, Zhang R H, Liu J B, Zhou A F, Feng S. 2019. Westerlies Asia and monsoonal Asia: Spatiotemporal differences in climate change and possible mechanisms on decadal to sub-orbital timescales. Earth-Sci Rev, 192: 337–354

Chen F H, Chen J H, Huang W. 2009. A discussion on the westerly-dominated climate model in mid-latitude Asia during the modern interglacial period (in Chinese). Earth Sci Front, 16: 23–32

Chen F H, Jia J, Chen J H, Li G Q, Zhang X J, Xie H C, Xia D S, Huang W, An C B. 2016. A persistent Holocene wetting trend in arid Central Asia, with wettest conditions in the late Holocene, revealed by multi-proxy analyses of loess-paleosol sequences in Xinjiang, China. Quat Sci Rev, 146: 134–146

Chen F H, Yu Z C, Yang M L, Ito E, Wang S M, Madsen D B, Huang X Z, Zhao Y, Sato T, Birks H J B, Boomer I, Chen J H, An C B, Wünnemann B. 2008. Holocene moisture evolution in arid Central Asia and its out-of-phase relationship with Asian monsoon history. Quat Sci Rev, 27: 351–364

Chen G S, Kutzbach J E, Gallimore R, Liu Z. 2011. Calendar effect on phase study in paleoclimate transient simulation with orbital forcing. Clim Dyn, 37: 1949–1960

Chen S Q, Chen J H, Lv F Y, Liu X K, Hou J Z, Chen F H. 2022. Holocene moisture variation in arid Central Asia: Reassessment and reconciliation. (submitted)

Cheng H, Spötl C, Breitenbach S F M, Sinha A, Wassenburg J A, Jochum K P, Scholz D, Li X L, Yi L, Peng Y B, Lv Y B, Zhang P Z, Votintseva A, Loginov V, Ning Y F, Kathayat G, Edwards R L. 2016. Climate variations of Central Asia on orbital to millennial timescales. Sci Rep, 6: 36975

D'Arrigo R, Jacoby G, Pederson N, Frank D, Buckley B, Nachin B, Mijiddorj R, Dugarjav C. 2000. Mongolian tree-rings, temperature sensitivity and reconstructions of Northern Hemisphere temperature. Holocene, 10: 669–672

Danabasoglu G, Lamarque J -, Bacmeister J, Bailey D A, DuVivier A K, Edwards J, Emmons L K, Fasullo J, Garcia R, Gettelman A, Hannay C, Holland M M, Large W G, Lauritzen P H, Lawrence D M, Lenaerts J T M, Lindsay K, Lipscomb W H, Mills M J, Neale R, Oleson K W, Otto-Bliesner B, Phillips A S, Sacks W, Tilmes S, Kampenhout L, Vertenstein M, Bertini A, Dennis J, Deser C, Fischer C, Fox-Kemper B, Kay J E, Kinnison D, Kushner P J, Larson V E, Long M C, Mickelson S, Moore J K, Nienhouse E, Polvani L, Rasch P J, Strand W G. 2020. The community earth system model version 2 (CESM2). J Adv Model Earth Syst, 12: e2019MS001916

Davis B A S, Brewer S, Stevenson A C, Guiot J. 2003. The temperature of Europe during the Holocene reconstructed from pollen data. Quat Sci Rev, 22: 1701–1716

Feng Z D, Sun A Z, Abdusalih N, Ran M, Kurban A, Lan B, Zhang D L, Yang Y P. 2017. Vegetation changes and associated climatic changes in the southern Altai Mountains within China during the Holocene. Holocene, 27: 683–693

Ferronskii V I, Polyakov V A, Brezgunov V S, Vlasova L S, Karpychev Y A, Bobkov A F, Romaniovskii V V, Johnson T, Ricketts D, Rasmussen K. 2003. Variations in the hydrological regime of Kara-Bogaz-Gol Gulf, Lake Issyk-Kul, and the Aral Sea assessed based on data of bottom sediment studies. Water Resources, 30: 252–259

Gasse F, Arnold M, Fontes J C, Fort M, Gibert E, Huc A, Li B Y, Li Y F, Li Q, Mélières F, Campo E V, Wang F B, Zhang Q S. 1991. A 13,000-year climate record from western Tibet. Nature, 353: 742–745

Guan X F, Yang L M, Zhang Y X, Li J G. 2019. Spatial distribution, temporal variation, and transport characteristics of atmospheric water vapor over Central Asia and the arid region of China. Glob Planet Change, 172: 159–178

Guo C C, Bentsen M, Bethke I, Ilicak M, Tjiputra J, Toniazzo T, Schwinger J, Otterå O H. 2019. Description and evaluation of NorESM1-F: A fast

version of the Norwegian Earth System Model (NorESM). Geosci Model Dev, 12: 343–362
He B, Bao Q, Wang X C, Zhou L J, Wu X F, Liu Y M, Wu G X, Chen K J, He S C, Hu W T, Li J D, Li J X, Nian G K, Wang L, Yang J, Zhang M H, Zhang X Q. 2019. CAS FGOALS-f3-L model datasets for CMIP6 historical atmospheric model intercomparison project simulation. Adv Atmos Sci, 36: 771–778
Hong B, Gasse F, Uchida M, Hong Y T, Leng X T, Shibata Y, An N, Zhu Y X, Wang Y. 2014. Increasing summer rainfall in arid eastern-Central Asia over the past 8500 years. Sci Rep, 4: 5279
Huang W, Chen F H, Feng S, Chen J H, Zhang X J. 2013. Interannual precipitation variations in the mid-latitude Asia and their association with large-scale atmospheric circulation. Chin Sci Bull, 58: 3962–3968
Huang X Z, Chen F H, Fan Y X, Yang M L. 2009. Dry late-glacial and early Holocene climate in arid Central Asia indicated by lithological and palynological evidence from Bosten Lake, China. Quat Int, 194: 19–27
Huang X Z, Peng W, Rudaya N, Grimm E C, Chen X M, Cao X Y, Zhang J, Pan X D, Liu S S, Chen C Z, Chen F H. 2018. Holocene vegetation and climate dynamics in the Altai Mountains and Surrounding Areas. Geophys Res Lett, 45: 6628–6636
Indermuhle A, Stauffer B, Stocker T F, Raynaud D, Barnola J M. 1999. Early Holocene atmospheric CO_2 concentrations. Science, 286: 1815
Jiang Q F, Ji J F, Shen J, Matsumoto R, Tong G B, Qian P, Ren X M, Yan D Z. 2013. Holocene vegetational and climatic variation in westerly-dominated areas of Central Asia inferred from the Sayram Lake in northern Xinjiang, China. Sci China Earth Sci, 56: 339–353
Jin L Y, Chen F H, Morrill C, Otto-Bliesner B L, Rosenbloom N. 2012. Causes of early Holocene desertification in arid Central Asia. Clim Dyn, 38: 1577–1591
Joussaume S, Braconnot P. 1997. Sensitivity of paleoclimate simulation results to season definitions. J Geophys Res, 102: 1943–1956
Kelley M, Schmidt G A, Nazarenko L S, Bauer S E, Ruedy R, Russell G L, Ackerman A S, Aleinov I, Bauer M, Bleck R, Canuto V, Cesana G, Cheng Y, Clune T L, Cook B I, Cruz C A, Del Genio A D, Elsaesser G S, Faluvegi G, Kiang N Y, Kim D, Lacis A A, Leboissetier A, LeGrande A N, Lo K K, Marshall J, Matthews E E, McDermid S, Mezuman K, Miller R L, Murray L T, Oinas V, Orbe C, García-Pando C P, Perlwitz J P, Puma M J, Rind D, Romanou A, Shindell D T, Sun S, Tausnev N, Tsigaridis K, Tselioudis G, Weng E, Wu J, Yao M S. 2020. GISS-E2.1: Configurations and climatology. J Adv Model Earth Syst, 12: e2019MS002025
Krivonogov S K, Kuzmin Y V, Burr G S, Gusskov S A, Khazin L B, Zhakov E Y, Nurgizarinov A N, Kurmanbaev R K, Kenshinbay T I. 2010. Environmental changes of the Aral Sea (Central Asia) in the Holocene: Major trends. Radiocarbon, 52: 555–568
Kutzbach J E, Chen G, Cheng H, Edwards R L, Liu Z. 2014. Potential role of winter rainfall in explaining increased moisture in the Mediterranean and Middle East during periods of maximum orbitally-forced insolation seasonality. Clim Dyn, 42: 1079–1095
Kutzbach J E, Liu X D, Liu Z Y, Chen G S. 2008. Simulation of the evolutionary response of global summer monsoons to orbital forcing over the past 280,000 years. Clim Dyn, 30: 567–579
Kutzbach J E, Otto-Bliesner B L. 1982. The sensitivity of the African-Asian monsoonal climate to orbital parameter changes for 9000 years B. P. in a low-resolution general circulation model. J Atmos Sci, 39: 1177–1188
Leroy S A G, López-Merino L, Tudryn A, Chalié F, Gasse F. 2014. Late Pleistocene and Holocene palaeoenvironments in and around the middle Caspian basin as reconstructed from a deep-sea core. Quat Sci Rev, 101: 91–110
Li J P, Wang J X L. 2003. A modified zonal index and its physical sense. Geophys Res Lett, 30: 1632
Li J Y, Wang N L, Dodson J, Yan H, Zhang X J, Jia P W, Seppa H. 2020. Holocene negative coupling of summer temperature and moisture availability over southeastern arid Central Asia. Clim Dyn, 55: 1187–1208
Li L J, Yu Y Q, Tang Y L, Lin P F, Xie J B, Song M R, Dong L, Zhou T J, Liu L, Wang L, Pu Y, Chen X L, Chen L, Xie Z H, Liu H B, Zhang L X, Huang X, Feng T, Zheng W P, Xia K, Liu H L, Liu J P, Wang Y, Wang L H, Jia B H, Xie F, Wang B, Zhao S W, Yu Z P, Zhao B W, Wei J L. 2020. The flexible global ocean-atmosphere-land system model grid-point version 3 (FGOALS-g3): Description and evaluation. J Adv Model Earth Syst, 12: e02012
Liu C L, Zhang J F, Jiao P C, Mischke S. 2016. The Holocene history of Lop Nur and its palaeoclimate implications. Quat Sci Rev, 148: 163–175
Liu X K, Liu J B, Shen C C, Yang Y, Chen J H, Chen S Q, Wang X F, Wu C C, Chen F H. 2020. Inconsistency between records of $\delta^{18}O$ and trace element ratios from stalagmites: Evidence for increasing mid-late Holocene moisture in arid central Asia. Holocene, 30: 369–379
Liu X K, Rao Z G, Shen C C, Liu J B, Chen J H, Chen S Q, Wang X F, Chen F H. 2019. Holocene solar activity imprint on centennial- to multidecadal-scale hydroclimatic oscillations in arid Central Asia. J Geophys Res-Atmos, 124: 2562–2573
Liu X Q, Herzschuh U, Shen J, Jiang Q F, Xiao X Y. 2008. Holocene environmental and climatic changes inferred from Wulungu Lake in northern Xinjiang, China. Quat Res, 70: 412–425
Liu Z Y, Wen X Y, Brady E C, Otto-Bliesner B, Yu G, Lu H Y, Cheng H, Wang Y J, Zheng W P, Ding Y H, Edwards R L, Cheng J, Liu W, Yang H. 2014. Chinese cave records and the East Asia Summer Monsoon. Quat Sci Rev, 83: 115–128
Liu Z, Otto-Bliesner B L, He F, Brady E C, Tomas R, Clark P U, Carlson A E, Lynch-Stieglitz J, Curry W, Brook E, Erickson D, Jacob R, Kutzbach J, Cheng J. 2009. Transient simulation of last deglaciation with a new mechanism for Bølling-Allerød warming. Science, 325: 310–314
Long H, Shen J, Chen J, Tsukamoto S, Yang L, Cheng H, Frechen M. 2017. Holocene moisture variations over the arid Central Asia revealed by a comprehensive sand-dune record from the central Tian Shan, NW China. Quat Sci Rev, 174: 13–32
Lorenz S J, Kim J H, Rimbu N, Schneider R R, Lohmann G. 2006. Orbitally driven insolation forcing on Holocene climate trends: Evidence from alkenone data and climate modeling. Paleoceanography, 21: PA1002
Loulergue L, Schilt A, Spahni R, Masson-Delmotte V, Blunier T, Lemieux B, Barnola J M, Raynaud D, Stocker T F, Chappellaz J. 2008. Orbital and millennial-scale features of atmospheric CH_4 over the past 800,000 years. Nature, 453: 383–386
Mauritsen T, Bader J, Becker T, Behrens J, Bittner M, Brokopf R, Brovkin V, Claussen M, Crueger T, Esch M, Fast I, Fiedler S, Fläschner D, Gayler V, Giorgetta M, Goll D S, Haak H, Hagemann S, Hedemann C, Hohenegger C, Ilyina T, Jahns T, Jimenéz-de-la-Cuesta D, Jungclaus J, Kleinen T, Kloster S, Kracher D, Kinne S, Kleberg D, Lasslop G, Kornblueh L, Marotzke J, Matei D, Meraner K, Mikolajewicz U, Modali K, Möbis B, Müller W A, Nabel J E M S, Nam C C W, Notz D, Nyawira S S, Paulsen H, Peters K, Pincus R, Pohlmann H, Pongratz J, Popp M, Raddatz T J, Rast S, Redler R, Reick C H, Rohrschneider T, Schemann V, Schmidt H, Schnur R, Schulzweida U, Six K D, Stein L, Stemmler I, Stevens B, von Storch J S, Tian F, Voigt A, Vrese P, Wieners K H, Wilkenskjeld S, Winkler A, Roeckner E. 2019. Developments in the MPI-M Earth system model version 1.2 (MPI-ESM1.2) and its response to increasing CO_2. J Adv Model Earth Syst, 11: 998–1038
Monnin E, Steig E J, Siegenthaler U, Kawamura K, Schwander J, Stauffer B, Stocker T F, Morse D L, Barnola J M, Bellier B, Raynaud D, Fischer H. 2004. Evidence for substantial accumulation rate variability in Antarctica during the Holocene, through synchronization of CO_2 in the Taylor Dome, Dome C and DML ice cores. Earth Planet Sci Lett, 224: 45–54
Montoya M, von Storch H, Crowley T J. 2000. Climate simulation for 125 kyr BP with a coupled ocean-atmosphere general circulation model. J Clim, 13: 1057–1072
Olsen J, Anderson N J, Knudsen M F. 2012. Variability of the North Atlantic Oscillation over the past 5,200 years. Nat Geosci, 5: 808–812
Orme L C, Miettinen A, Seidenkrantz M S, Tuominen K, Pearce C, Divine

D V, Oksman M, Kuijpers A. 2021. Mid to late-Holocene sea-surface temperature variability off north-eastern Newfoundland and its linkage to the North Atlantic Oscillation. Holocene, 31: 3–15
Prell W L, Kutzbach J E. 1987. Monsoon variability over the past 150,000 years. J Geophys Res, 92: 8411–8425
Rackow T, Goessling H F, Jung T, Sidorenko D, Semmler T, Barbi D, Handorf D. 2018. Towards multi-resolution global climate modeling with ECHAM6-FESOM. Part II: Climate variability. Clim Dyn, 50: 2369–2394
Rasmussen K A, Ricketts R D, Johnson T C, Romanovsky V V, Grigina O M. 2001. An 8,000 year multi-proxy record from Lake Issyk-Kul, Kyrgyzstan. PAGES News, 9: 5–6
Ricketts R D, Johnson T C, Brown E T, Rasmussen K A, Romanovsky V V. 2001. The Holocene paleolimnology of Lake Issyk-Kul, Kyrgyzstan: Trace element and stable isotope composition of ostracodes. Palaeogeogr Palaeoclimatol Palaeoecol, 176: 207–227
Rimbu N, Lohmann G, Kim J H, Arz H W, Schneider R. 2003. Arctic/North Atlantic Oscillation signature in Holocene sea surface temperature trends as obtained from alkenone data. Geophys Res Lett, 30: 1280
Rimbu N, Lohmann G, Lorenz S J, Kim J H, Schneider R R. 2004. Holocene climate variability as derived from alkenone sea surface temperature and coupled ocean-atmosphere model experiments. Clim Dyn, 23: 215–227
Ruddiman W F. 2007. Earth's Climate, Past, Future. 2nd ed. New York: W. H. Freeman and Company. 484
Seland Ø, Bentsen M, Olivié D, Toniazzo T, Gjermundsen A, Graff L S, Debernard J B, Gupta A K, He Y C, Kirkevåg A, Schwinger J, Tjiputra J, Aas K S, Bethke I, Fan Y, Griesfeller J, Grini A, Guo C, Ilicak M, Karset I H H, Landgren O, Liakka J, Moseid K O, Nummelin A, Spensberger C, Tang H, Zhang Z, Heinze C, Iversen T, Schulz M. 2020. Overview of the Norwegian Earth System Model (NorESM2) and key climate response of CMIP6 DECK, historical, and scenario simulations. Geosci Model Dev, 13: 6165–6200
Sidorenko D, Rackow T, Jung T, Semmler T, Barbi D, Danilov S, Dethloff K, Dorn W, Fieg K, Goessling H F, Handorf D, Harig S, Hiller W, Juricke S, Losch M, Schröter J, Sein D V, Wang Q. 2015. Towards multi-resolution global climate modeling with ECHAM6-FESOM. Part I: Model formulation and mean climate. Clim Dyn, 44: 757–780
Sorg A, Bolch T, Stoffel M, Solomina O, Beniston M. 2012. Climate change impacts on glaciers and runoff in Tien Shan (Central Asia). Nat Clim Change, 2: 725–731
Sun A Z, Feng Z D, Ran M, Zhang C J. 2013. Pollen-recorded bioclimatic variations of the last ~22,600 years retrieved from Achit Nuur core in the western Mongolian Plateau. Quat Int, 311: 36–43
Tao S C, An C B, Chen F H, Tang L Y, Wang Z L, Lü Y B, Li Z F, Zheng T M, Zhao J J. 2010. Pollen-inferred vegetation and environmental changes since 16.7 ka BP at Balikun Lake, Xinjiang. Chin Sci Bull, 55: 2449–2457
Tian F, Herzschuh U, Telford R J, Mischke S, Van der Meeren T, Krengel M. 2014. A modern pollen-climate calibration set from central-western Mongolia and its application to a late glacial-Holocene record. J Biogeogr, 41: 1909–1922
Volodin E M, Mortikov E V, Kostrykin S V, Galin V Y, Lykossov V N, Gritsun A S, Diansky N A, Gusev A V, Iakovlev N G, Shestakova A A, Emelina S V. 2018. Simulation of the modern climate using the INM-CM48 climate model. Rus J Numer Anal Math Model, 33: 367–374
Wang Q, Wei H T, Khormali F, Wang L B, Yan H Y, Xie H C, Wang X, Huang W, Chen J H, Chen F H. 2020. Holocene moisture variations in western arid Central Asia inferred from loess records from NE Iran. Geochem Geophys Geosyst, 21: e08616
Wang W, Feng Z D, Ran M, Zhang C J. 2013. Holocene climate and vegetation changes inferred from pollen records of Lake Aibi, northern Xinjiang, China: A potential contribution to understanding of Holocene climate pattern in East-central Asia. Quat Int, 311: 54–62
Wang W, Feng Z D. 2013. Holocene moisture evolution across the Mongolian Plateau and its surrounding areas: A synthesis of climatic records. Earth-Sci Rev, 122: 38–57
Wang W, Zhang D L. 2019. Holocene vegetation evolution and climatic dynamics inferred from an Ombrotrophic Peat sequence in the southern Altai Mountains within China. Glob Planet Change, 179: 10–22
Wu Z P, Yin Q Z, Guo Z T, Berger A. 2020. Hemisphere differences in response of sea surface temperature and sea ice to precession and obliquity. Glob Planet Change, 192: 103223
Wünnemann B, Mischke S, Chen F H. 2006. A Holocene sedimentary record from Bosten Lake, China. Palaeogeogr Palaeoclimatol Palaeoecol, 234: 223–238
Xie T T, Huang W, Feng S, Wang T, Liu Y, Chen J H, Chen F H. 2021. Mechanism of winter precipitation variations in the southern arid Central Asia. Int J Climatol, http://doi.org/10.1002/joc.7480
Xu H N, Wang T, Wang H J, Miao J P, Chen J H, Chen S Q. 2020. The PMIP3 simulated climate changes over Arid Central Asia during the Mid-Holocene and Last Glacial Maximum. Acta Geol Sin-Engl Ed, 94: 725–742
Xu H, Zhou K E, Lan J H, Zhang G L, Zhou X Y. 2019. Arid Central Asia saw mid-Holocene drought. Geology, 47: 255–258
Yuan X, Shi Z G, Zhou W J. 2014. North Atlantic Oscillation changes and its relationship with Asian precipitation in mid-Holocene and last glacial maximum: Results from MPI-ESM simulations (in Chinese). Quat Sci, 34: 1156–1156
Yukimoto S, Kawai H, Koshiro T, Oshima N, Yoshida K, Urakawa S, Tsujino H, Deushi M, Tanaka T, Hosaka M, Yabu S, Yoshimura H, Shindo E, Mizuta R, Obata A, Adachi Y, Ishii M. 2019. The meteorological research institute earth system model version 2.0, MRI-ESM2.0: Description and basic evaluation of the physical component. J Meteorol Soc Jpn, 97: 931–965
Zhang D L, Chen X, Li Y M, Ran M, Yang Y P, Zhang S R, Feng Z D. 2020. Holocene moisture variations in the Arid Central Asia: New evidence from the southern Altai Mountains of China. Sci Total Environ, 735: 139545
Zhang D L, Feng Z D. 2018. Holocene climate variations in the Altai Mountains and the surrounding areas: A synthesis of pollen records. Earth-Sci Rev, 185: 847–869
Zhang Q, Berntell E, Axelsson J, Chen J, Han Z, de Nooijer W, Lu Z, Li Q, Zhang Q, Wyser K, Yang S. 2021. Simulating the mid-Holocene, last interglacial and mid-Pliocene climate with EC-Earth3-LR. Geosci Model Dev, 14: 1147–1169
Zhang X J. 2021. Penetration of monsoonal water vapour into arid Central Asia during the Holocene: An isotopic perspective. Quat Sci Rev, 251: 106713
Zhang X J, Jin L Y, Chen J, Chen F H, Park W, Schneider B, Latif M. 2017. Detecting the relationship between moisture changes in arid Central Asia and East Asia during the Holocene by model-proxy comparison. Quat Sci Rev, 176: 36–50
Zhang X J, Jin L Y, Huang W, Chen F H. 2016. Forcing mechanisms of orbital-scale changes in winter rainfall over northwestern China during the Holocene. Holocene, 26: 549–555
Zhang X J, Jin L Y, Yu F, Wang Z Y. 2010. Mid-Holocene NAO: Based on PMIP2 model simulations (in Chinese). Acta Oceanol Sin, 32: 41–50
Zhang Y, Meyers P A, Liu X T, Wang G P, Ma X H, Li X Y, Yuan Y X, Wen B L. 2016. Holocene climate changes in the Central Asia mountain region inferred from a peat sequence from the Altai Mountains, Xinjiang, northwestern China. Quat Sci Rev, 152: 19–30
Zhang Y, Yang P, Tong C, Liu X T, Zhang Z Q, Wang G P, Meyers P A. 2018. Palynological record of Holocene vegetation and climate changes in a high-resolution peat profile from the Xinjiang Altai Mountains, northwestern China. Quat Sci Rev, 201: 111–123

(Responsible editor: Jianping HUANG)